Automatic ultrasound image segmentation based on local entropy and active contour model

Jing-jing Zong [a,b], Tian-shuang Qiu [a,*], Wei-dong Li [b], Dong-mei Guo [c]

[a] *Faculty of Electronic Information and Electrical Engineering, Dalian University of Technology, Dalian 116024, China*
[b] *School of Electrical & Information Engineering, Dalian Jiaotong University, Dalian 116028, China*
[c] *Department of Radiology, Second Affiliated Hospital, Dalian Medical University, Dalian 116027, China*

ARTICLE INFO

ABSTRACT

It is still a challenging task to segment ultrasound medical images automatically and accurately because of the poor quality of images. To address these problems, a two-stage automatic segmentation scheme based on local entropy and a proposed active contour model for ultrasound images are put forward in this paper. First, a new region-based active contour model in the level set formulation, driven by global and local intensity information, is established for the segmentation. Furthermore, for automatically segmenting the ultrasound images, a coarse segmentation is performed utilizing local entropy information of the ultrasound images, then the coarse segmentation result is used as the initial value of the explicit segmentation based on the proposed model. Several experiments on real ultrasound images demonstrate that the proposed method outperforms other methods on both visual perception and objective evaluation metrics.

© 2019 Published by Elsevier Ltd.

1. Introduction

Medical image segmentation is of great significance for three-dimensional visualization, three-dimensional location, image-guided intervention and surgery, quantitative analysis and computer-aided diagnosis [1]. Among various imaging techniques, ultrasound (US) imaging has been widely used clinically due to its non-invasiveness, painlessness, convenience, intuitiveness and effectiveness [2]. However, the automatic and accurate segmentation of the US images is still one of the research hotspots and difficulties due to their low signal-to-noise ratio (SNR), low contrast, attenuation, shadowing, and blurring boundaries [2,3].

Many medical image segmentation methods have been proposed in the literatures, including thresholding [4], clustering [5], Markov random field (MRF) [6,7], active contour model (ACM) [2,8–10], etc. Of which, the ACM is one of the important techniques for US image segmentation. The ACMs can be roughly classified as parametric active contour model (PACM) [11,12] and geometric active contour model (GACM) [13–16]. The PACM is usually represented explicitly as parameterized curve in a Lagrangian formulation [17]; while the GACM is generally represented implicitly as the zero level set of a higher dimensional function (level set function) which evolves according to an Eulerian formulation and is commonly referred to as level set method (LSM). PACM utilizes the internal and external force to guide the curve toward the object boundaries, but it cannot handle the topological changes like breaking and merging during deformation. To solve this problem, the LSMs have been proposed. LSM has many advantages over PACM, such as computationally simplicity and the ability to change curve topology in deformation process [17].

---

* Corresponding author.
   E-mail addresses: jjzonghit@126.com (J.-j. Zong), qiutsh@dlut.edu.cn (T.-s. Qiu).

GACM (LSM) can be categorized into edge-based methods [13,15,18,19], region-based methods [20–26] and hybrid GACMs [27–33]; where region-based methods can be roughly classified into global region-based methods [20] and local region-based methods [21–25]. Edge-based methods use image gradient function to evolve the contour toward object boundaries, they can segment images with intensity heterogeneity and work well for objects with good contrast, but tend to have the boundary leakage problem for indistinct or gapped object boundary. In addition, they are sensitive to noises and initial contours. Region-based methods identify each region by a specific region descriptor to drive the active contour evolution, compared with edge-based methods, region-based methods perform better on weak boundaries and they are usually less sensitive to noises and initial contours. However, the global region-based method, such as the typical CV model [20] which based on Mumford–Shah [34] and level set method, has some inherent limitations. For example, since such piecewise constant (PC) model is based on the assumption of image intensity homogeneity, it fails to segment images with intensity heterogeneity; meanwhile, the initial contour location and initial parameters still affect the final segmentation result for complex images [30].

To segment intensity heterogeneous images, in addition to the edge-based model (e.g.: GAC [15]) mentioned above and the piecewise smooth (PS) models [35,36] based on Mumford–Shah model, many local region-based methods have been proposed [8,22–25,29]. Among them, the RSF model [22], which was originally called LBF model in [21], incorporates the local image information via using a kernel function and exceeds the PS models [35,36] in both efficiency and accuracy [21]; based on the RSF model, many local models were born. Specially, the LGDF model [23] assumes that the local image intensity obeys the Gaussian distribution of different means and variances, it can handle intensity inhomogeneity and Gaussian noise while with high computational time; the LIF model [24] uses a Gaussian low-pass filtered image to fit the original image, its segmentation result is comparable to LBF while with higher efficiency; the LCK model [25] introduces the correntropy criterion [37] to the objective function instead of the commonly used mean square error (MSE) criterion to solve the segmentation under complex noise, it is robust to noise and can segment images accurately; the LIC model [8] proposes a framework which can simultaneously segment the intensity heterogeneous image and estimate the bias field.

Although the local region-based methods can segment intensity heterogeneous images, their curves evolve more slowly, resulting in lower segmentation efficiency. To quickly and efficiently segment images, some hybrid GACMs which combined global and local region-based models were proposed [27–33]. Of these, LGIF [28] is the most classic and representative one. Inspired by these works, taking into account the characteristics of US images, we propose a novel hybrid region-based active contour model (named as GLM) based on global and local information for US image interactive segmentation; furthermore, we propose an automatic segmentation framework based on the proposed GLM and local entropy.

The highlights of this paper can be listed as follows.

• The GLM model is built by incorporating global and local information in a variational level set formulation, so that it can combine the advantages of global and local models, making the level set quickly and accurately approach the target boundary under the combined effect of global forces and local forces. Specially, our global term and CV model have some equivalence, it can be considered as a special case of CV model; the local term is equivalent to a narrowband implementation, thus improving the computational efficiency.

• An automated segmentation framework is proposed to achieve automatic segmentation for US images, it overcomes the disadvantages of non-convex model in sensitivity to initial values.

• The local entropy feature is used to perform US image coarse segmentation. As far as we know, this is the first attempt to use local entropy in US image automatic segmentation framework.

The remainder of the paper is organized as follows. Some common or related ACMs in this field are briefly reviewed in Section 2. The proposed GLM for US interactive segmentation is introduced in Section 3. The proposed automatic segmentation framework is introduced in Section 4. The experimental results and discussions are given in Section 5. Finally, we summarize this paper and discuss future research in Section 6.

2. Brief review of related work

2.1. CV model

CV model is proposed by Chan and Vese [20], it assumes the image to be segmented is a piecewise constant (PC) function and is suitable for segmenting intensity homogeneity image. Given image $I: \Omega \subset R^2 \to R$, level set function ϕ, the contour $C = x \in \Omega: \phi(x) = 0$ is supposed to segment I into two homogeneous regions $\Omega_1 = x \in \Omega: \phi(x) > 0$ and $\Omega_2 = x \in \Omega: \phi(x) < 0$, with mean values c_1 and c_2, respectively. For pixel $x \in \Omega$, the CV model transforms segmentation problem into the minimization of the following energy functional:

$$E^{CV}(\phi, c_1, c_2) = \lambda_1 \int_{inside(C)} |I(x) - c_1|^2 H(\phi(x))dx + \lambda_2 \int_{outside(C)} |I(x) - c_2|^2 (1 - H(\phi(x))dx) + \nu |C| \tag{1}$$

where $|C|$ denotes the length of C, $\lambda_1 > 0$, $\lambda_2 > 0$ (usually take $\lambda_1 = \lambda_2 = 1$) and $\nu \geq 0$ are the weighting coefficients for the data fidelity/fitting terms (the first two terms in Eq. (1)) and regularized length term, respectively. $H(\phi(\cdot))$ is the Heaviside function (also known as step function) and its approximated expression is usually used. For more details, the reader can refer to paper [20].

2.2. RSF (or LBF) model

The RSF model [22] (also called LBF model [21]) is proposed by Li et al. [21,22], which can segment image with intensity inhomogeneity. Its energy functional is:

$$E^{RSF}(\phi, \mu_1, \mu_2) = \sum_{i=1}^{2} \lambda_i \iint K_\sigma(y-x) |I(x) - \mu_i(y)|^2 M_i(\phi(x)) \, dxdy + E_r \tag{2}$$

where the symbol λ_i has the same meaning as mentioned in CV model; $M_i(\phi(x))$ is a region membership function composed of Heaviside function; $K_\sigma(\cdot)$ is the Gaussian kernel/window function with standard deviation σ, theoretically, the role of the Gaussian kernel/mask is to perform Gaussian low-pass filtering on the original image $I(x)$ to obtain a fitting image $\mu_i(y)$, so the value of σ should be selected properly, when the noise or intensity inhomogeneity is large, a larger σ should be selected, and vice visa. E_r is the regularization term including length term and the distance regularizing term. For more details, the interesting reader can refer to [21,22].

2.3. LGIF model

The LGIF model is proposed by Wang et al. [28], which combines CV model and RSF model linearly to expect the advantages of both. The energy functional is as follows:

$$E^{LGIF}(\phi, c_1, c_2, \mu_1, \mu_2) = wE^{CV}(\phi, c_1, c_2)_{\text{data}} + (1-w)E^{RSF}(\phi, \mu_1, \mu_2)_{\text{data}} + E_r \tag{3}$$

where w is a weighting constant ($0 \leq w \leq 1$), the regularization term E_r has the same meaning as mentioned in RSF model. $E^{CV}(\phi, c_1, c_2)_{\text{data}}$, $E^{RSF}(\phi, \mu_1, \mu_2)_{\text{data}}$ represent data fidelity terms of CV model and RSF model, respectively. For more details, the reader can refer to paper [28].

3. Proposed active contour model

In this section, we proposed an active contour model named GLM model for US segmentation. The proposed model includes two parts: the data fitting term E_d and the regularization term E_r. Motivated by active contour model which uses both global and local information [28,29,31,33], the data fitting term includes the global energy term E_g and the local energy term E_l. The energy functional is formulated as:

$$E = E_d + E_r = wE_g + (1-w)E_l + E_r \tag{4}$$

where w is a weighting constant ($0 \leq w \leq 1$) between E_g and E_l.

3.1. Data fitting term

3.1.1. Global energy term
Let $I: \Omega \subset \mathrm{R}^2 \to \mathrm{R}$ denote the image to be segmented, a closed evolving curve $C \subset \Omega$, which is represented by the zero level set of level set function ϕ, i.e., $C = x \in \Omega: \phi(x) = 0$, is used to separate the image domain Ω into two regions: $\Omega_1 = x \in \Omega: \phi(x) > 0$ and $\Omega_2 = x \in \Omega: \phi(x) < 0$, the two regions can be distinguished by some region statistics such as sample mean or variance [20,38–41]. Inspired by both the work of Yezzi [38–41] and the OTSU method [42], taking into account the characteristics of ultrasound images, we propose to evolve contour C by maximizing the between-class distance. For any pixel coordinate $x \in \Omega \subset \mathrm{R}^2$, an average global energy functional we employed is to minimize the following:

$$E_{g1} = -P_{g1}P_{g2}(c_1 - c_2)^2 \tag{5}$$

Different from those proposed by Yezzi et al. [38–41], the prior probability information is incorporated into our model to help the segmentation algorithm extract the region of interest. The image statistics used here are as follows:

area in Ω_1: $A_{g1} = \int_\Omega H(\phi(x)) \, dx$

area in Ω_2: $A_{g2} = \int_\Omega [1 - H(\phi(x))] \, dx$

area in Ω: $A_g = \int_\Omega dx$

sum of intensity in Ω_1: $S_{g1} = \int_\Omega I(x) H(\phi(x)) \, dx$

sum of intensity in Ω_2: $S_{g2} = \int_\Omega I(x) [1 - H(\phi(x))] \, dx$

probability of class occurrence in Ω_1: $P_{g1} = \frac{A_{g1}}{A_g} = \frac{\int_\Omega H(\phi(x))dx}{\int_\Omega dx}$

probability of class occurrence in Ω_2: $P_{g2} = \frac{A_{g2}}{A_g} = \frac{\int_\Omega [1 - H(\phi(x))]dx}{\int_\Omega dx}$
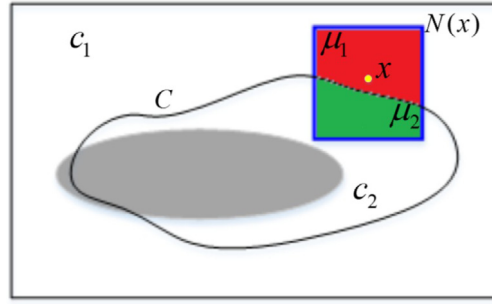
Fig. 1. Schematic diagram of evolution curve under global and local constraints.

average intensity in

$$\Omega_1 : c_1 = \frac{S_{g1}}{A_{g1}} = \frac{\int_\Omega I(x) H(\phi(x)) \, dx}{\int_\Omega H(\phi(x)) \, dx} \tag{6}$$

average intensity in

$$\Omega_2 : c_2 = \frac{S_{g2}}{A_{g2}} = \frac{\int_\Omega I(x) [1 - H(\phi(x))] \, dx}{\int_\Omega [1 - H(\phi(x))] \, dx} \tag{7}$$

where the Heaviside step function H is given by $H(\phi(x)) = \begin{cases} 1, & if \ \phi(x) \geq 0 \\ 0, & if \ \phi(x) < 0 \end{cases}$, in actual application, $H(\phi(x))$ is approximated by a smooth function $H_\varepsilon(\phi) = \frac{1}{2}\left[1 + \frac{2}{\pi}\arctan\left(\frac{\phi}{\varepsilon}\right)\right]$, the derivative of H_ε is $\delta_\varepsilon(\phi) = H'_\varepsilon(\phi) = \frac{1}{\pi}\frac{\varepsilon}{\varepsilon^2 + \phi^2}$, which is an approximation of the Dirac function $\delta(\phi)$, where $\varepsilon > 0$ is a constant, $\varepsilon = 1$ is used in this paper.

The aim of the global energy term is to minimize E_{g1} for all the pixels x, which guides us to define the following total global energy functional:

$$E_g = \int_\Omega E_{g1} dx \tag{8}$$

Minimizing the energy functional (8) with respect to ϕ by gradient descent method (see Appendix A), we can get that:

$$\frac{\partial \phi_g}{\partial t} = -\frac{\partial E_g}{\partial \phi} = \delta(c_1 - c_2)(2I - c_1 - c_2) \tag{9}$$

From Eq. (9), it can be seen that the solution of the global term E_g is the same as the data fidelity term of the CV model when $\lambda_1 = \lambda_2 = 1$ in Eq. (1), that is, our global term and CV model share the same goal and have some equivalence, our global term can be considered as a special case of CV model.

3.1.2. Local energy term

Recently, local intensity information is incorporated into active contour models for more accurate segmentation [21–25]. In this section, we will discuss the local energy functional that differentiates regions based on the local average intensities. As shown in Fig. 1, $N(x) \triangleq y: |y - x| \leq r_y$ (r_y is the radius between x and y, y is an independent spatial variable in $N(x)$) represents a local neighborhood region centered at x, its shape can be rectangular, circular, etc. The localized equivalents of c_1 and c_2, μ_1 and μ_2, represent the local intensity means inside and outside the curve C, respectively. Following the way in Refs. [24,29,38–41,43–46], the local means are defined empirically by a window function, e.g. a truncated Gaussian kernel/mask w_σ with standard deviation σ [21,22,24] (for more details, see [22] etc.), as follows:

$$\mu_1(x) = \frac{S_{l1}}{A_{l1}} = \frac{\int w_\sigma(x-y) I(y) H(\phi(y)) \, dy}{\int w_\sigma(x-y) H(\phi(y)) \, dy} = \frac{w_\sigma(x) * [I(x) H(\phi(x))]}{w_\sigma(x) * H(\phi(x))} \tag{10}$$

$$\mu_2(x) = \frac{S_{l2}}{A_{l2}} = \frac{\int w_\sigma(x-y) I(y) [1 - H(\phi(y))] \, dy}{\int w_\sigma(x-y) [1 - H(\phi(y))] \, dy} = \frac{w_\sigma(x) * [I(x)(1 - H(\phi(x)))]}{w_\sigma(x) * [1 - H(\phi(x))]} \tag{11}$$

where $*$ is convolution operator, $\mu_1(x)$ and $\mu_2(x)$ can be regarded as the weighted averages of image intensities in N_1 and N_2 (see Appendix B), respectively.

The local energy functional is motivated by the same consideration as global energy functional, that is, we achieve more accurate segmentation by maximizing the distance between μ_1 and μ_2. The corresponding local energy at each point along the curve C is formed by localizing the global energy with local statistic equivalents as shown here:

$$E_{l1} = -P_{l1}P_{l2}(\mu_1 - \mu_2)^2 \tag{12}$$

The local statistics used in (12) are given by:

$$P_{l1} = \frac{A_{l1}}{A_l} = \frac{\int_{N(x)} w_\sigma \, (x - y) \, H \, (\phi(y)) \, dy}{\int_{N(x)} w_\sigma \, (x - y) \, dy} \tag{13}$$

$$P_{l2} = \frac{A_{l2}}{A_l} = \frac{\int_{N(x)} w_\sigma \, (x - y) \, [1 - H \, (\phi(y))] \, dy}{\int_{N(x)} w_\sigma \, (x - y) \, dy} \tag{14}$$

where the parameters A_{l1}, A_{l2}, A_l, S_{l1}, S_{l2}, P_{l1}, P_{l2}, μ_1, μ_2 are the localized versions of their globalization parameters A_{g1}, A_{g2}, A_g, S_{g1}, S_{g2}, P_{g1}, P_{g2}, c_1, c_2, respectively. These corresponding parameters have the same geometric meaning, except for the global or local differences. Some local parameter expressions are no longer listed here (see Appendix B), the reader can refer to their corresponding global expressions above.

For $x \in N(x)$, the entire local narrowband energy E_l is achieved by minimizing the integral of E_{l1} over the image domain $N(x)$, namely,

$$E_l = \int_{N(x)} E_{l1} dx \tag{15}$$

Minimizing the energy functional (15) with respect to ϕ by gradient descent method (see Appendix B):

$$\frac{\partial \phi_l}{\partial t} = -\frac{\partial E_l}{\partial \phi} = (\mu_1 - \mu_2)\,[2 \, (w * \delta I) - w \delta \cdot (\mu_1 + \mu_2)] \tag{16}$$

From (15), it can be seen that our local term is equivalent to a narrowband implementation, thus improving the computational efficiency.

3.2. Regularization term

As with the typical active contour model, the widely adopted regularization term E_r proposed in [22] is exploited here, which includes two parts: the level set regularization term $P(\phi)$ and the length term $L(\phi)$.

$$E_r = \mu P(\phi) + \nu L(\phi) \tag{17}$$

where $\mu > 0$, $\nu > 0$ are positive constants, which control the length penalization effect and signed distance function (SDF) maintaining effect.

3.2.1. Level set regularization term

$$P(\phi) = \int_\Omega \frac{1}{2} \, (|\nabla \phi \, (x)| - 1)^2 \, dx \tag{18}$$

This term penalizes the deviation of the level set function ϕ from SDF, for more details see [18].

3.2.2. Length term

$$L(\phi) = |C| = \int_\Omega |\nabla H \, (\phi \, (x))| \, dx = \int_\Omega \delta \, (\phi \, (x)) \, |\nabla \phi \, (x)| \, dx \tag{19}$$

As in most of level set methods (LSMs), this term smooths the contour C by penalizing its length $|C|$, it forces $|C|$ as short as possible, aiming to avoid the emergence of small and isolated curves in the final segmentation result [30].

3.3. Energy minimization

The optimal active contour $\phi^*(t)$ is defined as

$$\phi^*(t) = \arg \min_\phi \{E(\phi(x))\} \tag{20}$$

where the energy functional $E(\phi) = wE_g + (1 - w)E_l + \mu P(\phi) + \nu L(\phi)$. Obviously, function $E(\phi)$ is a linear combination of functions E_g, E_l, $P(\phi)$ and $L(\phi)$, since all these four functions are non-negative, the optimization problem represented by Eq. (20) can be rewritten as:

$$\phi^*(t) = w \cdot \arg \min_\phi E_g + (1 - w) \cdot \arg \min_\phi E_l + \mu \cdot \arg \min_\phi P(\phi) + \nu \cdot \arg \min_\phi L(\phi) \tag{21}$$
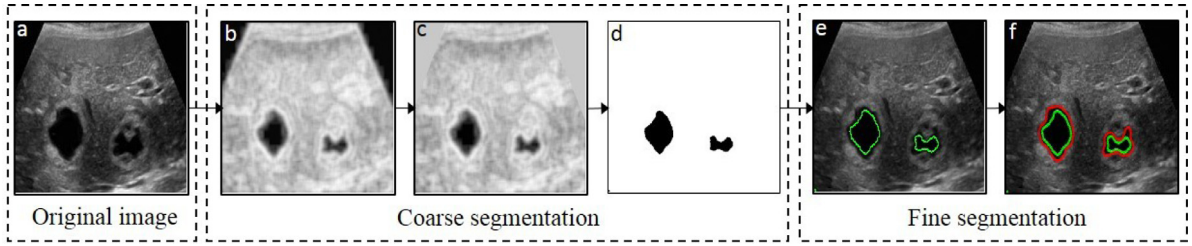
Fig. 2. Graphical representation of the proposed method . (For interpretation of the references to color in this figure legend, the reader is referred to the web version of this article.)

The minimization of $E(\phi)$ with respect to ϕ can be achieved by using standard gradient descent method:

$$\frac{\partial \phi}{\partial t} = -\frac{\partial E}{\partial \phi} \tag{22}$$

The corresponding gradient flow equation is (refer to Appendices A and B):

$$\frac{\partial \phi}{\partial t} = \underbrace{\underbrace{w\,[\delta_\varepsilon\,(\phi)\,(c_1 - c_2)(2I - c_1 - c_2)]}_{\text{global term}} + (1-w)\underbrace{\{(\mu_1 - \mu_2)\,[2\,(w * \delta_\varepsilon I) - w\delta_\varepsilon \cdot \mu_1 - w\delta_\varepsilon \cdot \mu_2]\}}_{\text{local term}}}_{\text{data term}}$$

$$+ \underbrace{\mu\left[\nabla^2\phi - div\left(\frac{\nabla\phi}{|\nabla\phi|}\right)\right] + v\delta_\varepsilon\,(\phi)\,div\left(\frac{\nabla\phi}{|\nabla\phi|}\right)}_{\text{regularization term}} \tag{23}$$

where ∇ is gradient operator, $div(\cdot)$ is divergence operator, $*$ is convolution operator, $w\delta_\varepsilon = w_\sigma\,(x) * \delta_\varepsilon\,(\phi(x))$, $\delta_\varepsilon I = I\,(x) \cdot \delta_\varepsilon\,(\phi(x))$. Approximating $\frac{\partial\phi}{\partial t}$ by the forward difference, Eq. (23) can be written as

$$\phi_{n+1} = \phi_n + \Delta t \cdot G(\phi_n) \tag{24}$$

where $G(\phi_n)$ represents the right side of Eq. (23), Δt is the time step.

3.4. Algorithm steps

Step 1: Initialize the level set function ϕ to a binary step function, that is, $\phi(x, t = 0) = \begin{cases} r & x \in \text{inside}(C) \\ -r & \text{otherwise} \end{cases}$, where $r > 0$ is a constant;

Step 2: Initialize the parameters for level set evolution, e.g. the iteration number, r, μ, v, w, σ, the time step, ε, etc.

Step 3: Update global and local means according to Eqs. (6), (7), (10) and (11);

Step 4: Update the level set function ϕ using Eq. (24).

Step 5: Terminate iteration if the convergence is reached, or else return to step 3.

In this section, we proposed an ACM for US interactive segmentation. Like most active contour models, our model is non-convex, the segmentation result depends on the shape and location of the initial contour, or else it is easy to fall into local minimum. To avoid falling into the local minimum and realize automated and accurate US segmentation, we propose a scheme in Section 4.

4. Proposed scheme for automatic US segmentation

In this section, our algorithm aims to realize a computerized automatic segmentation of the US image, we go about this task with a local entropy-based algorithm which consists of two stages (Fig. 2): the coarse segmentation stage where the local entropy image of the US image is segmented using OTSU thresholding method [42]; the fine segmentation stage where the explicit segmentation is implemented via the proposed active contour model. However, it should be pointed out that other suitable region-based models can also be applied to this framework. The details and major contributions are introduced in the following sections.

4.1. Coarse segmentation

4.1.1. Feature selection: why choose local entropy?

Image segmentation can be viewed as the classification of all the image pixels into different clusters that have similar features. To perform coarse segmentation, we need to first identify informative features from the image. While the

choice of features is still an open problem. Commonly used features include the pixel intensity, color, gradient, texture, etc. [47,48]. Features directly from the input image is not suitable for our problem due to the low resolution, low contrast as well as the influence of intrinsic speckle noises in US medical images. Different from the traditional method, taking into account the characteristic of US images, our coarse segmentation is performed on the local entropy image (see Fig. 2(c)) instead of the original intensity image (see Fig. 2(a)). The heuristic idea of using local entropy as the feature comes from the fact that the local entropy has been proved to be robust to irradiation distortion, geometric distortion and noise interference [49,50]. As indicated by Fig. 2(c), the local entropy image computed in a neighborhood is roughly representative of the underlying local data structure. Comparing Fig. 2(a) with Fig. 2(c), it can be seen that the gray level is more sensitive to local gray variations, while the local entropy is relatively stable to local gray deformations. So we can use local entropy to distinguish between goals and background here.

In information theory, entropy is sometimes referred to as Shannon entropy [51]. Shannon's probabilistic entropy is defined as the average information of a probability distribution. Local entropy is derived by calculating the entropy in a local region of the image, which describes the statistical characteristics of the region. The local entropy of pixel i can be computed by

$$E(i) = -\sum_{g=1}^{N} P(g) \log_2 P(g) \tag{25}$$

where $E(i)$ is the image entropy on ith pixel, $P(g)$ is the probability of gray level g in the neighborhood of pixel i, N is the image gray level. Local entropy reflects the variance and heterogeneity within the neighborhood, from Eq. (25) we can see that the local entropy is large for regions with uniform distribution of gray levels, but small for regions with uneven gray scale distribution.

4.1.2. Coarse segmentation steps

Step 1: Compute the local entropy matrix E of the original image by Eq. (25) (corresponding image representation of E is shown in Fig. 2(b)), using a 9×9 neighborhood centered on each pixel i.

Step 2: Detect vignetting in the upper left corner and upper right corner of the local entropy E (as shown in Fig. 2(b)), then remove the vignetting by making $E(i) = C$ in the vignetting area, where C is a constant ($C \leq n$ for n-bit image, here $n = 8$) and is recommended an empirical value of 5 here.

Step 3: Generate a local entropy image E_{im} (as shown in Fig. 2(c)) by converting the local entropy E to a grayscale image, where the values $E(i)$ are linearly transformed between 0 and 255, i.e. $E_{im}(i) \in [0, 255]$. The conversion formula is as follows:

$$E_{im}(i) = \frac{E(i) - \min E(i)}{\max E(i) - \min E(i)} \times 255 \tag{26}$$

Step 4: Perform segmentation on local entropy image E_{im} by OTSU thresholding method, obtain the coarse segmentation result (as shown in Fig. 2(d) and the green curves in Fig. 2(e)).

4.2. Fine segmentation

Ref. [52] reports that the infrared image segmentation based on local entropy may bring target range diffusion and result in false detection. We found in the experiment that the coarse segmentation based on local entropy will cause shrinkage of the target area and false detection (see Figs. 2(e)–(f)). So a resoluble procedure is proposed for precise segmentation, which is called fine segmentation. The steps are as follows:

Step 1: Use the coarse segmentation result as the initial contour of the original image (green curves shown in Fig. 2(e)).

Step 2: Perform explicit segmentation based on the proposed GLM model to obtain the segmentation result (red curves shown in Fig. 2(f)).

5. Experiments

In this section, experiments on nine representative ultrasound medical images are presented to evaluate the effectiveness of the method. The nine images are shown in the first row in Fig. 3, from I_1 to I_9, followed by breast cyst, renal cyst, hydatid cyst and intramural nodule, bronchus, intrahepatic portal vein, gall bladder, cholecystitis, femoral artery, liquefied hematoma. More ultrasound image data can be found from the database (http://www.ultrasound-images.com, http://www.radiologyinfo.org). All the experiments were implemented in Matlab R2015b on Intel(R) @3.60 GHz 3.60 GHz CPU with 16GB RAM and Windows 10 Operating System.

Here, the same parameters used in all experiments are set as follows: $\Delta t = 0.1$, $\mu = 1$, $\varepsilon = 1$. Due to the complexity of the US image, other parameters are adjusted according to different images. It should be noted that because the role of the Gaussian kernel w_σ is to perform Gaussian low-pass filtering on the original image to obtain the fitting image, the value of σ should be selected properly, when the noise or intensity inhomogeneity is large, a larger σ should be selected, and vice visa. Meanwhile, the weighting constant $w(0 \leq w \leq 1)$ should be set according to the degree of intensity inhomogeneity. When the inhomogeneity of the image is large, the local energy term will play a major role in the segmentation result, then w should be set to a small value, and vice versa.
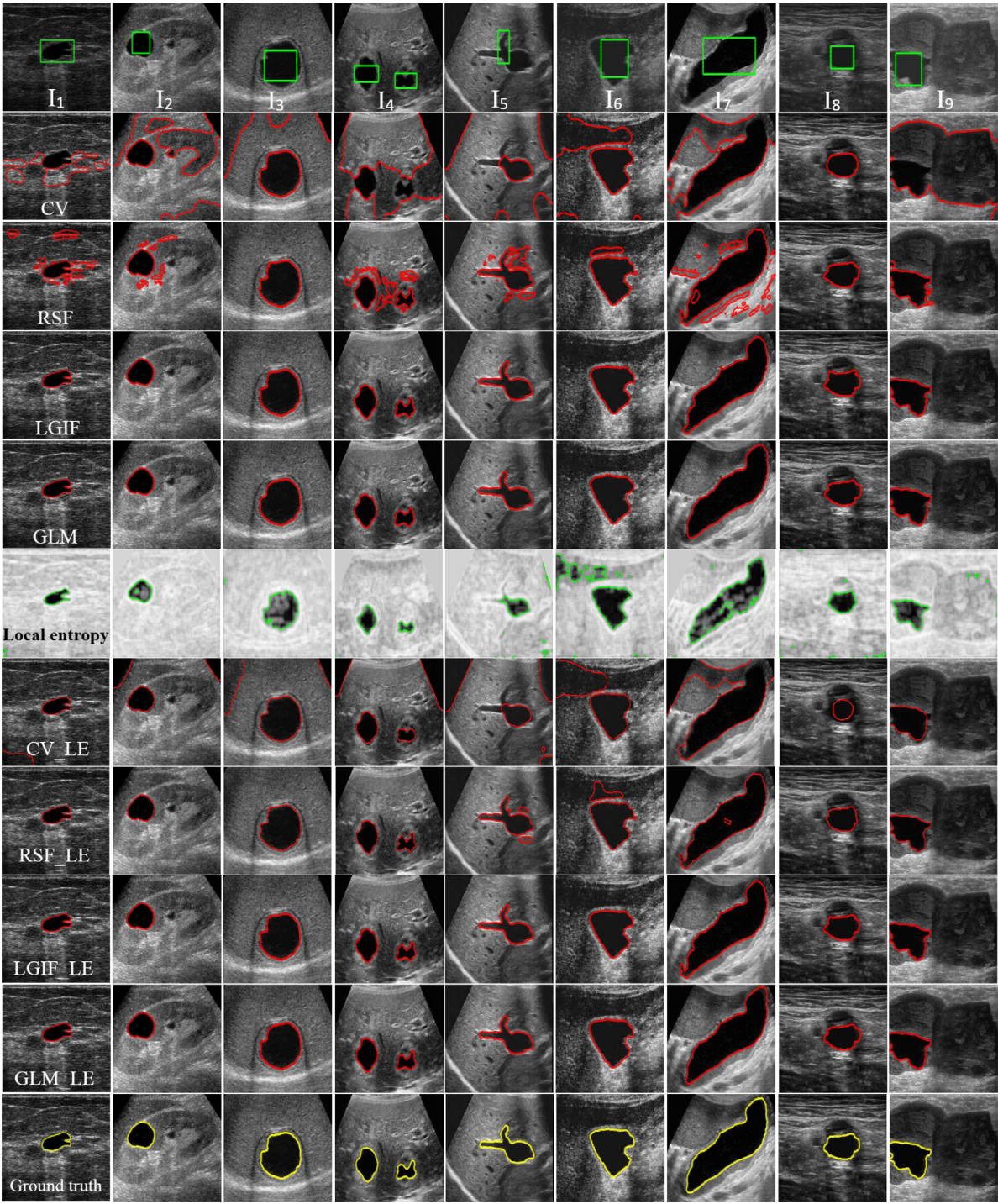
Fig. 3. Segmentation results obtained by different methods. Row 1: original images and initial contours (green rectangles); Row 2 to 5: segmentation results of CV model, RSF model, LGIF model and the proposed GLM model (red curves); Row 6: local entropy images and their coarse segmentation results by OTSU method (green curves); Row 7 to 10: segmentation results of CV_LE, RSF_LE, LGIF_LE methods and the proposed GLM_LE method (red curves); Row 11: The ground truth (yellow curves). (For interpretation of the references to color in this figure, the reader is referred to the web version of this paper).

5.1. Objective evaluation metrics and the ground truth

In addition to subjective evaluation, there are several quantitative metrics to evaluate segmentation performance, such as the false positive (FP) [53], true positive (TP) [53], Dice similarity coefficient (DSC) [54], Hausdorff distance (HD) [55,56], Jaccard similarity index (JSI) [57], etc. The objective evaluation criteria are not uniform, multiple evaluation indices are usually selected for proper evaluation. Three performance metrics are used in this work, they are defined as follows:

DSC is one of the most widely used quantitative indicators for evaluating segmentation accuracy, it measures the overlap between the segmentation result and the ground truth. Let S_g and S_m be the binary mask of ground truth and the computerized segmentation method, the DSC is computed by

$$DSC(S_g, S_m) = \frac{2\left|S_g \cap S_m\right|}{\left|S_g\right| + \left|S_m\right|} \tag{27}$$

JSI is another region-based metric used for comparing the similarity of sample sets, which is given as

$$JSI(S_g, S_m) = \frac{\left|S_g \cap S_m\right|}{\left|S_g \cup S_m\right|} \tag{28}$$

The boundary-based, nonlinear operator HD measures how far the computerized delineated boundary from the ground truth, for the given two finite point set S_g and S_m, the max–min distance HD is defined as

$$HD(S_g, S_m) = \max\left(\max_{s_g \in S_g} d(s_g), \max_{s_m \in S_m} d'(s_m)\right) \tag{29}$$

where $d(x) = \min_{s_m \in S_m} \|x - s_m\|$, $d'(x) = \min_{s_g \in S_g} \|s_g - x\|$, $\| \cdot \|$ denotes Euclidean norm, we can obtain $HD(S_g, S_m)$ by calculating $d(s_g)$ and $d'(s_m)$ for all $s_g \in S_g$ and $s_m \in S_m$, respectively.

Of these three metrics, a higher value of DSC or JSI and a lower HD value indicate better segmentation performance with respect to the ground truth.

According to the above description, in order to evaluate the quality of image segmentation, the true boundary of the target should be determined. However, the fact is, there is no ground truth available without histopathologic samples, which is a major challenge in the field of medical segmentation [54]. Instead, some surrogate truths such as manual delineation are often used. In this work, follow the idea of STAPLE method [58], all of the ground truth are estimated by weighting the segmentation results of 3 expert observers.

5.2. Experimental results and discussion

5.2.1. Experiment 1: Evaluation of the GLM model

The first experiment is performed to estimate the performance of the GLM model proposed in Section 3. In this semi-automatic segmentation experiment, the proposed model GLM is evaluated on nine representative US images. As described in step 1 of Section 3.4, the initial contour is manually initialized to a rectangular ROI (see the green curve in the first row of Fig. 3). Three representative ACMs including CV model [20], RSF model [22] and LGIF model [28] are compared with our model, the final segmentation results of CV model, RSF model, LGIF model and the proposed model GLM are sequentially shown in the second to the fifth rows of Fig. 3, and the ground truth are shown in the last row of Fig. 3.

From the subjective perspective, it can be seen from the second row of Fig. 3 that the CV model produces severe over-segmentation and false segmentation in 8 images, the reason is that the CV model only uses global information to segment image which is difficult to handle images with inhomogeneous intensity; The third row of Fig. 3 demonstrates that fewer over-segmentation appeared in 7 images by the RSF model, the reason is because the local region-based RSF model only uses local image information which may capture more image details for complex US image; The results of LGIF model and the proposed GLM model are shown in the fifth and sixth rows of Fig. 3, respectively, it can be observed that both models outperform others due to the use of both global and local information. The segmentation results of the both are subjectively close to the ground truth, except for the seventh experiment, as shown in the 4th row, 7th column and the 5th row, 7th column of Fig. 3, the segmentation curve of the LGIF method is not as smooth as that of GLM method.

In addition to subjective visual comparison, from the objective perspective, three objective metrics listed in the left part of Table 1 are used to compare the LGIF and GLM models, and the running times for both models are shown in Table 2. The numbers in brackets refer to the number of relevant methods obtained the first place. From the left part of Table 1, it can be seen that, for a single experiment, the difference in DSC or JSI coefficients between the two models is very small. And there is small difference in HD coefficients between the two models except for the seventh experiment, in which the HD coefficient of the LGIF method is larger than that of GLM method, which indicates a better match between the GLM method and the gold standard (ground truth), and this is consistent with our above-mentioned subjective difference about the seventh experiment. Finally, in terms of the mean value, specially, it can be seen that for both DSC and JSI, the performance of GLM method is the best, but the difference between the two methods is not obvious. On the whole, the three indicators of the GLM method are slightly better than the LGIF method.

Table 1
Objective assessment of the LGIF, GLM, LGIF_LE and GLM_LE methods. Best result of the 2 methods in Experiment 1 or 2 is in bold, best result of the 4 methods is in red bold. (For interpretation of the references to color in this table, the reader is referred to the web version of this paper.)

Metrics	DSC		HD		JSI		DSC		HD		JSI	
Method	LGIF	GLM	LGIF	GLM	LGIF	GLM	LGIF_LE	GLM_LE	LGIF_LE	GLM_LE	LGIF_LE	GLM_LE
I_1	0.9816	**0.9848**	0.1654	**0.1336**	0.9639	**0.9700**	0.9800	**0.9854**	0.1714	**0.1501**	0.9608	**0.9713**
I_2	0.9837	**0.9855**	**0.1706**	0.2029	0.9679	**0.9713**	0.9796	**0.9844**	0.1883	**0.1816**	0.9601	**0.9694**
I_3	**0.9931**	0.9861	**0.2312**	0.3658	**0.9862**	0.9726	**0.9931**	0.9847	**0.2414**	0.3637	**0.9862**	0.9699
I_4	**0.9666**	0.9637	**0.4388**	0.4465	**0.9354**	0.9300	0.9679	**0.9840**	0.4482	**0.3286**	0.9378	**0.9686**
I_5	0.9717	**0.9875**	0.3798	**0.2298**	0.9449	**0.9754**	0.9743	**0.9897**	0.3291	**0.1521**	0.9499	**0.9796**
I_6	**0.9848**	0.9791	**0.3951**	0.5004	**0.9701**	0.9591	**0.9863**	0.9741	**0.3197**	0.5892	**0.9730**	0.9495
I_7	0.9768	**0.9900**	1.2539	**0.7767**	0.9547	**0.9802**	0.9730	**0.9878**	1.3804	**0.8760**	0.9474	**0.9758**
I_8	0.9671	**0.9742**	**0.2958**	0.3006	0.9363	**0.9497**	0.9747	**0.9756**	0.2860	**0.2816**	0.9507	**0.9523**
I_9	**0.9829**	0.9822	**0.3000**	0.3599	**0.9663**	0.9651	0.9845	**0.9983**	0.3049	**0.0537**	0.9695	**0.9966**
mean±	0.9787	**0.9815**	0.4034	**0.3685**	0.9584	**0.9637**	0.9793	**0.9849**	0.4077	**0.3307**	0.9595	**0.9703**
std	±	±	±	±	±	±	±	±	±	±	±	±
	0.0089	0.0081	0.3332	0.1926	0.0170	0.0156	0.0078	0.0072	0.3739	0.2577	0.0149	0.0140

Table 2
Running time of the LGIF, GLM, LGIF_LE and GLM_LE methods. Best result of the 2 methods in Experiment 1 or 2 is in bold, best result of the 4 methods is in red bold. Very few outliers are marked blue. (For interpretation of the references to color in this table, the reader is referred to the web version of this paper.).

Method	LGIF	GLM	LGIF_LE	GLM_LE
Images	time(s)/iterations	time(s)/iterations	time(s)/iterations	time(s)/iterations
I_1	**1.2894**/50	1.3905/140	**1.7812**/40	2.0407/50
I_2	3.3314/300	**1.4109**/150	2.2156/80	**1.8404**/70
I_3	3.6389/260	**0.7863**/65	2.3002/120	**0.8882**/45
I_4	2.5486/140	**1.3993**/90	**1.7215**/40	2.4754/50
I_5	12.98/720	**4.7527**/260	4.9637/220	**3.4676**/200
I_6	2.7123/280	**2.0539**/170	**1.5828**/80	**11.4881/600**
I_7	9.4713/800	**3.8044**/600	6.1384/340	**1.2786**/60
I_8	2.3543/200	**1.1808**/110	2.0608/100	**1.1406**/70
I_9	1.5048/90	**1.0731**/100	1.4571/60	**1.0605**/60
mean±std	4.4256±4.0244(1)	**1.9835**±1.3655(3)	**2.6913**±1.6712(1)	2.8533±3.3402(4)

The 2nd column and the 3rd column of Table 2 list the running time of the LGIF and GLM methods, it can be seen from the table that the average computational efficiency of our method is higher than that of LGIF method. This is because our local energy term is equivalent to calculating the narrowband region near the contour, while the LGIF model takes the whole image region into account.

From the above subjective and objective comparisons and analyses, it can be seen that the LGIF and GLM methods are superior to other methods and they are comparable. But it should be noted that like most ACMs, both models are non-convex, so the segmentation results often depend on the initial contour. To further reduce the variation caused by this and realize the automatic segmentation, an automatic US segmentation scheme has been proposed in Section 4, and the experiment results are demonstrated in the following Section 5.2.2.

5.2.2. Experiment 2: Evaluation of the automatic US segmentation scheme

This experiment is performed to assess the performance of the proposed automatic US segmentation scheme. As described in Section 4.1.2, the initial contour is obtained from the local entropy image (see the green curve in 6th row of

Fig. 3 for each image), and the proposed GLM model is compared with the CV, RSF and LGIF models. Their results, labeled as GLM_LE, CV_LE, RSF_LE and LGIF_LE, are shown in the seventh and tenth rows of Fig. 3, respectively. The ground truth results are shown in the last row of Fig. 3. The corresponding objective metrics of algorithm LGIF_LE and GLM_LE are shown in the right part of Table 1, their running times are shown in the fourth column and the fifth column of Table 2, respectively.

Subjectively, it can be seen from Fig. 3 that in Experiment 2, since the local entropy image contour is used as the a priori guidance, the segmentation results of each model are improved. For example, the CV_LE algorithm gets approximate correct segmentation results in some cases, such as the 8th and 9th columns of the 7th row in Fig. 3, that is, the segmentation results of CV_LE on I_8 and I_9. RSF_LE algorithm improves more obviously, compared with CV_LE, its segmentation accuracy is higher, the segmentation results are more accurate at details; but there are still over-segmentation phenomena for individual complex images, such as the segmentation of I_5, I_6 and I_7 by this algorithm. In contrast, the segmentation results of both the LGIF_LE and the GLM_LE algorithms are better. Except for the seventh experiment, as shown in the 9th row, 7th column and the 10th row, 7th column of Fig. 3, the segmentation result of the LGIF_LE method suffers from a slight boundary leakage in the lower left of the weak boundary.

Objectively, it can be seen from the right part of Table 1 that there is little difference between the DSC or JSI coefficient, that is, the difference between these two objective indicators is not significant. And the HD coefficient of the GLM_LE method is less than that of the LGIF_LE method, which indicates that the mismatch degree between the GLM_LE model and the gold standard is low, i.e., the proposed model is well matched with the ground truth. The running times for both models are shown in the 4th and the 5th column of Table 2, it can be seen from the table that the average running time of the LGIF_LE is less than that of GLM_LE, but there is little difference between the two mean values. In fact, in most cases, the proposed method is computationally efficient, except for the 6th experiment, in which the computational time of the GLM_LE model is much longer than the LGIF_LE model (see the blue bold value in Table 2), which reduces the overall average of the proposed method. The time-consuming reason of the 6th experiment is that the pre-segmented result of the sixth image is far from its ground truth (compare the 6th row, 6th column with the 11th row, 6th column in Fig. 3), in this case, if the local entropy image is first smoothed (which consumes extra time), the result of the pre-segmentation will be closer to the ground truth (which usually leads to accelerated convergence and saves time). On the whole, although the method based on local entropy takes time due to pre-segmentation, when the pre-segmentation curve is close to the ground truth, the convergence speed of the algorithm is accelerated and the overall time is saved, and vice versa.

5.2.3. Overall comparison

In this subsection, for each method, the relevant contents in Fig. 3, Tables 1 and 2 are comprehensively considered to find some common regularities among the above two experiments. Subjectively, it can be seen from Fig. 3 that the segmentation results of the four algorithms including LGIF, GLM, LGIF_LE and GLM_LE are overall good, basically matching the shape of the gold standard. Among them, the method based on local entropy is superior to the non-local entropy method in keeping details. Objectively, from the last row of Table 1, it can be concluded that in terms of the average of objective performance indicators, there are: GLM_LE>GLM in all indicators, LGIF_LE>LGIF in DSC and JSI, LGIF_LE≈LGIF in HD, where the symbol '>' stands for surpass, '≈' represents approximate. These results demonstrate that the three objective performance indexes based on the local entropy method outperform the non-local entropy based method. The reason is that the initial contour of the local entropy based method is usually closer to the ground truth, so the segmentation result is better. Meanwhile, from Table 2, it can be observed that in terms of the average of running time, there are: GLM based method > LGIF based method, i.e., our proposed method runs faster than the LGIF based method. The reason lies in that our local term is equivalent to calculating the narrowband region near the level set contour, while LGIF calculates the whole region.

6. Conclusions

In this paper, a new automatic US segmentation scheme based on local entropy and proposed ACM is put forward. Specially, we first build a global and local based ACM by simultaneously maximizing the distance between classes globally and locally, the model is used to semi-automatically segment US images in experiment 1; then, based on the proposed model and the local entropy feature image of the US image, we achieved automatic segmentation of the US image in experiment 2. The experiments on different US images indicate that both the proposed model and the proposed automatic segmentation scheme appear to be competitive with the representative segmentation method in segmentation quality and computational efficiency, which could help to analyze US images.

Nevertheless, this work is only a preliminary attempt and there is plenty of room for improvement. For example, due to the limitation of dataset used in the experiment and the complexity of the US image, resulting in the chosen local entropy feature may not be applicable to an arbitrary US image, hence the choice of features remains an open problem. Furthermore, it is worth studying the applicability of the automatic segmentation scheme to other types of images, such as infrared images. At last, this scheme is expected to be used as a useful method in practical clinical applications such as ultrasound surgery navigation.

Acknowledgments

Appendix A. Global energy term and its solution

The following details are given from two aspects: modeling and solution.

A.1. Modeling

The global energy functional term is defined as:

$$E_g = \int_\Omega E_{g1} dx = A_g E_{g1}$$

The parameters used here are as follows:
For any pixel $x \in \Omega \subset R^2$, an average global energy functional is $E_{g1} = -P_{g1} P_{g2} (c_1 - c_2)^2$
area in Ω_1: $A_{g1} = \int_\Omega H(\phi(x)) \, dx$
area in Ω_2: $A_{g2} = \int_\Omega [1 - H(\phi(x))] \, dx$
area in Ω: $A_g = \int_\Omega dx$
sum of intensity in Ω_1: $S_{g1} = \int_\Omega I(x) H(\phi(x)) \, dx$
sum of intensity in Ω_2: $S_{g2} = \int_\Omega I(x) [1 - H(\phi(x))] \, dx$
probability of class occurrence in Ω_1: $P_{g1} = \frac{A_{g1}}{A_g} = \dfrac{\int_\Omega H(\phi(x)) \, dx}{\int_\Omega dx}$
probability of class occurrence in Ω_2: $P_{g2} = \frac{A_{g2}}{A_g} = \dfrac{\int_\Omega [1 - H(\phi(x))] \, dx}{\int_\Omega dx}$
average intensity in Ω_1: $c_1 = \frac{S_{g1}}{A_{g1}} = \dfrac{\int_\Omega I(x) H(\phi(x)) \, dx}{\int_\Omega H(\phi(x)) \, dx}$
average intensity in Ω_2: $c_2 = \frac{S_{g2}}{A_{g2}} = \dfrac{\int_\Omega I(x) [1 - H(\phi(x))] \, dx}{\int_\Omega [1 - H(\phi(x))] \, dx}$

The global segmentation problem is transformed into the minimization of Eq. (8), the optimal global level set $\phi_g^*(t)$ is defined as

$$\phi_g^*(t) = \arg \min_\phi \{ E_g(\phi(x)) \}$$

A.2. Solution

Minimizing the energy functional (8) with respect to ϕ by gradient descent method, we can get that:

$$\frac{\partial \phi_g}{\partial t} = -\frac{\partial E_g}{\partial \phi}$$

To solve the above equation, calculate the following partial derivatives:

$$\frac{\partial P_{g1}}{\partial \phi} = \frac{\int \delta(\phi(x)) \, dx}{A_g} = \frac{\delta(\phi(x))}{A_g} = \frac{\delta}{A_g}, \quad \frac{\partial P_{g2}}{\partial \phi} = \frac{-\int \delta(\phi(x)) \, dx}{A_g} = \frac{-\delta(\phi(x))}{A_g} = -\frac{\delta}{A_g};$$

$$\frac{\partial c_1}{\partial \phi} = \frac{S_{g1}' A_{g1} - S_{g1} A_{g1}'}{A_{g1}^2} = \frac{S_{g1}' - c_1 A_{g1}'}{A_{g1}} = \delta \cdot \frac{I - c_1}{A_{g1}}, \text{ similarly, we can get } \frac{\partial c_2}{\partial \phi} = -\delta \cdot \frac{I - c_2}{A_{g2}};$$

Based on the above, we have

$$\frac{\partial E_{g1}}{\partial \phi} = -\left(\frac{\partial P_{g1}}{\partial \phi} P_{g2} + P_{g1} \frac{\partial P_{g2}}{\partial \phi} \right)(c_1 - c_2)^2 - 2P_{g1} P_{g2}(c_1 - c_2)\left(\frac{\partial c_1}{\partial \phi} - \frac{\partial c_2}{\partial \phi} \right) = -\frac{\delta}{A_g}(c_1 - c_2)(2I - c_1 - c_2),$$

$$\frac{\partial E_g}{\partial \phi} = -\delta(c_1 - c_2)(2I - c_1 - c_2);$$

So the solution is: $\dfrac{\partial \phi_g}{\partial t} = -\dfrac{\partial E_g}{\partial \phi} = \delta(c_1 - c_2)(2I - c_1 - c_2)$.

Appendix B. Local energy term and its solution

B.1. Modeling

The local energy functional term is defined as:

$$E_l = \int_{N(x)} E_{l1} dx$$

The parameters used here are as follows:

The local energy at the point along the curve C is $E_{l1} = -P_{l1}P_{l2}(\mu_1 - \mu_2)^2$

Assuming the evolving curve C separates $N(x)$ into two regions: $N_1 = y \in N(x) : \phi(y) > 0$ and $N_2 = y \in N(x) : \phi(y) < 0$, then:

area in N_1: $A_{l1} = \int_{N(x)} w_\sigma (x - y) H (\phi(y)) dy$

area in N_2: $A_{l2} = \int_{N(x)} w_\sigma (x - y) [1 - H (\phi(y))] dy$

area in $N(x)$: $A_l = \int_{N(x)} w_\sigma (x - y) dy$

sum of intensity in N_1: $S_{l1} = \int_{N(x)} w_\sigma (x - y) I (y) H (\phi(y)) dy$

sum of intensity in N_2: $S_{l2} = \int_{N(x)} w_\sigma (x - y) I (y) [1 - H (\phi(y))] dy$

probability of class occurrence in N_1: $P_{l1} = \dfrac{A_{l1}}{A_l} = \dfrac{\int_{N(x)} w_\sigma (x - y) H (\phi(y)) dy}{\int_{N(x)} w_\sigma (x - y) dy}$

probability of class occurrence in N_2: $P_{l2} = \dfrac{A_{l2}}{A_l} = \dfrac{\int_{N(x)} w_\sigma (x - y) [1 - H (\phi(y))] dy}{\int_{N(x)} w_\sigma (x - y) dy}$

average intensity in N_1: $\mu_1 (x) = \dfrac{S_{l1}}{A_{l1}} = \dfrac{\int w_\sigma (x - y) I (y) H (\phi(y)) dy}{\int w_\sigma (x - y) H (\phi(y)) dy} = \dfrac{w_\sigma(x) * [I (x) H (\phi(x))]}{w_\sigma(x) * H (\phi(x))}$

average intensity in N_2: $\mu_2 (x) = \dfrac{S_{l2}}{A_{l2}} = \dfrac{\int w_\sigma (x - y) I (y) [1 - H (\phi(y))] dy}{\int w_\sigma (x - y) [1 - H (\phi(y))] dy} = \dfrac{w_\sigma(x) * [I (x) (1 - H (\phi(x)))]}{w_\sigma(x) * [1 - H (\phi(x))]}$

The local segmentation problem is transformed into the minimization of Eq. (15), the optimal local level set $\phi_l^*(t)$ is defined as

$$\phi_l^*(t) = \arg \min_\phi \{E_l(\phi(x))\}$$

B.2. Solution

Minimizing the energy functional (15) with respect to ϕ by gradient descent method, we can get that:

$$\frac{\partial \phi_l}{\partial t} = -\frac{\partial E_l}{\partial \phi}$$

To solve the above equation, calculate the following partial derivatives:

$$\frac{\partial P_{l1}}{\partial \phi} = \frac{\int w_\sigma (x - y) \delta (\phi(y)) dy}{A_l} = \frac{w_\sigma (x) * \delta (\phi(x))}{w_\sigma (x) * 1} = \frac{w\delta}{wone}, \text{ in the same way, } \frac{\partial P_{l2}}{\partial \phi} = \frac{-w\delta}{wone}, \text{where } wone = w_\sigma (x) * \mathbf{1}$$

($\mathbf{1}$ denotes a constant matrix with value 1);

$$\frac{\partial \mu_1}{\partial \phi} = \frac{S_{l1}' A_{l1} - S_{l1} A_{l1}'}{A_{l1}^2} = \frac{S_{l1}' - \mu_1 A_{l1}'}{A_{l1}} = \frac{\int w_\sigma (x - y) I (y) \delta (\phi(y)) dy - \mu_1 \cdot \int w_\sigma (x - y) \delta (\phi(y)) dy}{\int w_\sigma (x - y) H (\phi(y)) dy}, \text{ in the same way,}$$

$$= \frac{w_\sigma (x) * [I (x) \delta (\phi(x))] - \mu_1 \cdot [w_\sigma (x) * \delta (\phi(x))]}{w_\sigma (x) * H (\phi(x))} = \frac{w * \delta I - \mu_1 \cdot w\delta}{wH}$$

we can obtain

$$\frac{\partial \mu_2}{\partial \phi} = -\frac{w * \delta I - \mu_2 \cdot w\delta}{wone - wH};$$

Based on the above, we have

$$\frac{\partial E_{l1}}{\partial \phi} = -\left(\frac{\partial P_{l1}}{\partial \phi} P_{l2} + P_{l1}\frac{\partial P_{l2}}{\partial \phi}\right)(\mu_1 - \mu_2)^2 - 2P_{l1}P_{l2}(\mu_1 - \mu_2)\left(\frac{\partial \mu_1}{\partial \phi} - \frac{\partial \mu_2}{\partial \phi}\right) = -\frac{(\mu_1 - \mu_2)}{wone}\left[2\left(w * \delta I\right) - w\delta \cdot (\mu_1 + \mu_2)\right];$$

$$\frac{\partial E_l}{\partial \phi} = A_l \frac{\partial E_{l1}}{\partial \phi} = -(\mu_1 - \mu_2)\left[2\left(w * \delta I\right) - w\delta \cdot (\mu_1 + \mu_2)\right];$$

So the solution is: $\dfrac{\partial \phi_l}{\partial t} = -\dfrac{\partial E_l}{\partial \phi} = (\mu_1 - \mu_2)\left[2\left(w * \delta I\right) - w\delta \cdot (\mu_1 + \mu_2)\right].$

References

[1] J.A. Noble, D. Boukerroui, Ultrasound image segmentation: A survey, IEEE Trans. Med. Imaging 25 (2006) 987–1010.
[2] D. Gupta, R.S. Anand, A hybrid edge-based segmentation approach for ultrasound medical images, Biomed. Signal Process. Control 31 (2017) 116–126.
[3] L. Fang, T. Qiu, Y. Liu, C. Chen, Active contour model driven by global and local intensity information for ultrasound image segmentation, Comput. Math. Appl. 75 (2018) 4286–4299.
[4] P.K. Saha, J.K. Udupa, Optimum image thresholding via class uncertainty and region homogeneity, IEEE Trans. Pattern Anal. Mach. Intell. 23 (2001) 689–706.
[5] C.-C. Lai, C.-Y. Chang, A hierarchical evolutionary algorithm for automatic medical image segmentation, Expert Syst. Appl. 36 (2009) 248–259.
[6] J. Nie, Z. Xue, T. Liu, G.S. Young, K. Setayesh, L. Guo, S.T. Wong, Automated brain tumor segmentation using spatial accuracy-weighted hidden Markov random field, Comput. Med. Imaging Graph. 33 (2009) 431–441.
[7] Y. Zhang, M. Brady, S. Smith, Segmentation of brain MR images through a hidden Markov random field model and the expectation-maximization algorithm, IEEE Trans. Med. Imaging 20 (2001) 45–57.
[8] C. Li, R. Huang, Z. Ding, J.C. Gatenby, D.N. Metaxas, J.C. Gore, A level set method for image segmentation in the presence of intensity inhomogeneities with application to MRI, IEEE Trans. Image Process. 20 (2011) 2007–2016.
[9] E. Ilunga-Mbuyamba, J.M. Cruz-Duarte, J.G. Avina-Cervantes, C.R. Correa-Cely, D. Lindner, C. Chalopin, Active contours driven by cuckoo search strategy for brain tumour images segmentation, Expert Syst. Appl. 56 (2016) 59–68.
[10] J. Yuan, Active contour driven by region-scalable fitting and local Bhattacharyya distance energies for ultrasound image segmentation, IET Image Process. 6 (2012) 1075–1083.
[11] M. Kass, A. Witkin, D. Terzopoulos, Snakes: Active contour models, Int. J. Comput. Vis. 1 (1988) 321–331.
[12] L.D. Cohen, On active contour models and balloons, CVGIP: Image Underst. 53 (1991) 211–218.
[13] V. Caselles, F. Catté, T. Coll, F. Dibos, A geometric model for active contours in image processing, Numer. Math. 66 (1993) 1–31.
[14] R. Malladi, J.A. Sethian, B.C. Vemuri, Shape modeling with front propagation: A level set approach, IEEE Trans. Pattern Anal. Mach. Intell. 17 (1995) 158–175.
[15] V. Caselles, R. Kimmel, G. Sapiro, Geodesic active contours, Int. J. Comput. Vis. 22 (1997) 61–79.
[16] A. Yezzi, S. Kichenassamy, A. Kumar, et al., A geometric snake model for segmentation of medical imagery, IEEE Trans. Med. Imaging 16 (1997) 199–209.
[17] C. Xu, A. Yezzi, J.L. Prince, On the relationship between parametric and geometric active contours, signals, systems and computers, in: Conference Record of the Thirty-Fourth Asilomar Conference on, vol. 1, IEEE, 2000, pp. 483–489.
[18] C. Li, C. Xu, C. Gui, M.D. Fox, Level set evolution without re-initialization: A new variational formulation, in: Computer Vision and Pattern Recognition, 2005. CVPR 2005, in: IEEE Computer Society Conference on., vol. 1, IEEE, 2005, pp. 430–436.
[19] C. Li, C. Xu, C. Gui, M.D. Fox, Distance regularized level set evolution and its application to image segmentation, IEEE Trans. Image Process. 19 (2010) 3243–3254.
[20] T.F. Chan, L.A. Vese, Active contours without edges, IEEE Trans. Image Process. 10 (2001) 266–277.
[21] C. Li, C.-Y. Kao, J.C. Gore, Z. Ding, Implicit active contours driven by local binary fitting energy, in: Computer Vision and Pattern Recognition, 2007 CVPR '07, in: IEEE Conference on, IEEE, 2007, pp. 1–7.
[22] C. Li, C.Y. Kao, J.C. Gore, Z. Ding, Minimization of region-scalable fitting energy for image segmentation, IEEE Trans. Image Process. 17 (2008) 1940–1949.
[23] L. Wang, L. He, A. Mishra, C. Li, Active contours driven by local Gaussian distribution fitting energy, Signal Process. 89 (2009) 2435–2447.
[24] K. Zhang, H. Song, L. Zhang, Active contours driven by local image fitting energy, Pattern Recognit. 43 (2010) 1199–1206.
[25] L. Wang, C. Pan, Robust level set image segmentation via a local correntropy-based K-means clustering, Pattern Recognit. 47 (2014) 1917–1925.
[26] L. Wang, Y. Chang, H. Wang, Z. Wu, J. Pu, X. Yang, An active contour model based on local fitted images for image segmentation, Inf. Sci. 418 (2017) 61–73.
[27] S. Ali, A. Madabhushi, An integrated region- boundary- shape-based active contour for multiple object overlap resolution in histological imagery, IEEE Trans. Med. Imaging 31 (2012) 1448–1460.
[28] L. Wang, C. Li, Q. Sun, et al., Active Contours driven by local and global intensity fitting energy with application to brain MR image segmentation, Comput. Med. Imaging Graph. 33 (2009) 520–531.
[29] D. Li, W. Li, Q. Liao, Active contours driven by local and global probability distributions, J. Vis. Commun. Image Represent. 24 (2013) 522–533.
[30] X.-F. Wang, L. Zou, L.-X. Xu, G. Lv, C. Tang, Hybrid level set method based on image diffusion, Neurocomputing 228 (2017) 53–64.
[31] S. Zhou, J. Wang, S. Zhang, Y. Liang, Y. Gong, Active contour model based on local and global intensity information for medical image segmentation, Neurocomputing 186 (2016) 107–118.
[32] C.-y. Yu, W.-s. Zhang, Y.-y. Yu, Y. Li, A novel active contour model for image segmentation using distance regularization term, Comput. Math. Appl. 65 (2013) 1746–1759.
[33] C. Huang, L. Zeng, Robust image segmentation using local robust statistics and correntropy-based K-means clustering, Opt. Lasers Eng. 66 (2015) 187–203.
[34] D. Mumford, J. Shah, Optimal approximations by piecewise smooth functions and associated variational problems, Commun. Pure Appl. Math. 42 (1989) 577–685.
[35] A. Tsai, A. Yezzi, A.S. Willsky, Curve evolution implementation of the Mumford-Shah functional for image segmentation, denoising, interpolation, and magnification, IEEE Trans. Image Process. 10 (2001) 1169–1186.

[36] L.A. Vese, T.F. Chan, A multiphase level set framework for image segmentation using the mumford and shah model, Int. J. Comput. Vis. 50 (2002) 271–293.

[37] W. Liu, P.P. Pokharel, J.C. Principe, Correntropy: Properties and applications in non-Gaussian signal processing, IEEE Trans. Signal Process. 55 (2007) 5286–5298.

[38] A. Yezzi, A. Tsai, A. Willsky, Medical image segmentation via coupled curve evolution equations with global constraints, in: Mathematical Methods in Biomedical Image Analysis, 2000, in: Proceedings. IEEE Workshop on, IEEE, 2000, pp. 12–19.

[39] A. Yezzi, A. Tsai, A. Willsky, A fully global approach to image segmentation via coupled curve evolution equations, J. Vis. Commun. Image Represent 13 (2002) 195–216.

[40] A. Yezzi, A. Tsai, A. Willsky, A statistical approach to snakes for bimodal and trimodal imagery, computer vision, 1999, in: The Proceedings of the Seventh IEEE International Conference on, IEEE, 1999, pp. 898–903.

[41] A. Tsai, A. Yezzi Jr., W. Wells, C. Tempany, D. Tucker, A. Fan, W.E. Grimson, A. Willsky, A shape-based approach to the segmentation of medical imagery using level sets, IEEE Trans. Med. Imaging 22 (2003) 137–154.

[42] N. Otsu, A threshold selection method from gray-level histograms, IEEE Trans. Syst. Man Cybern. 9 (1979) 62–66.

[43] S. Lankton, A. Tannenbaum, Localizing region-based active contours, IEEE Trans. Image Process. 17 (2008) 2029–2039.

[44] T. Brox, From pixels to regions: Partial differential equations in image analysis, in: Diss, 2005.

[45] B. Rosenhahn, T. Brox, J. Weickert, Three-dimensional shape knowledge for joint image segmentation and pose estimation, Int. J. Comput. Vis. 73 (2007) 243–262.

[46] T. Brox, D. Cremers, On the statistical interpretation of the piecewise smooth mumford-shah functional, in: International Conference on Scale Space and Variational Methods in Computer Vision, Springer, Berlin, Heidelberg, 2007, pp. 203–213.

[47] P. Chatterjee, P. Milanfar, Clustering-based denoising with locally learned dictionaries, IEEE Trans. Image Process. 18 (2009) 1438–1451.

[48] M. Gong, Y. Liang, J. Shi, W. Ma, J. Ma, Fuzzy C-means clustering with local information and kernel metric for image segmentation, IEEE Trans. Image Process. 22 (2013) 573–584.

[49] Y. Zimmer, S. Akselrod, R. Tepper, The distribution of the local entropy in ultrasound images, Ultrasound Med. Biol. 22 (1996) 431–439.

[50] J. Barba, H. Jeanty, P. Fenster, J. Gil, The use of local entropy measures in edge detection for cytological image analysis, J. Microsc. 156 (1989) 125–134.

[51] C.E. Shannon, A mathematical theory of communication, Bell Syst. Tech. J. 27 (1948) 379–423.

[52] H. Deng, J. Liu, Z. Chen, Infrared small target detection based on modified local entropy and EMD, Chin. Opt. Lett. 8 (2010) 24–28.

[53] J.K. Udupa, V.R. Leblanc, Y. Zhuge, C. Imielinska, H. Schmidt, L.M. Currie, B.E. Hirsch, J. Woodburn, A framework for evaluating image segmentation algorithms, Comput. Med. Imaging Graph. 30 (2006) 75–87.

[54] B. Foster, U. Bagci, A. Mansoor, Z. Xu, D.J. Mollura, A review on segmentation of positron emission tomography images, Comput. Biol. Med. 50 (2014) 76–96.

[55] D.P. Huttenlocher, G.A. Klanderman, W.J. Rucklidge, Comparing images using the hausdorff distance, IEEE Trans. Pattern Anal. Mach. Intell. 15 (1993) 850–863.

[56] M.-P. Dubuisson, A.K. Jain, A modified hausdorff distance for object matching, in: Pattern Recognition, 1994 1-Conference a: Computer Vision & Image Processing, in: Proceedings of the 12th IAPR International Conference on, vol. 1, IEEE, 1994, pp. 566–568.

[57] J.K. Udupa, V.R. LaBlanc, H. Schmidt, et al., A methodology for evaluating image-segmentation algorithms medical imaging 2002: Image processing, Int. Soci. Opt. Photonics 4684 (2002) 266–278.

[58] S.K. Warfield, K.H. Zou, W.M. Wells, Simultaneous truth and performance level estimation (STAPLE): An algorithm for the validation of image segmentation, IEEE Trans. Med. Imaging 23 (2004) 903–921.